

ARTICLE

<https://doi.org/10.1038/s41467-019-12326-y>

OPEN

Synthesis of clathrate cerium superhydride CeH_9 at 80-100 GPa with atomic hydrogen sublattice

Nilesh P. Salke¹, M. Mahdi Davari Esfahani², Youjun Zhang³, Ivan A. Kruglov^{4,5}, Jianshi Zhou⁶, Yaguo Wang⁶, Eran Greenberg⁷, Vitali B. Prakapenka⁷, Jin Liu¹, Artem R. Oganov^{8,4,9*} & Jung-Fu Lin^{10*}

Hydrogen-rich superhydrides are believed to be very promising high- T_c superconductors. Recent experiments discovered superhydrides at very high pressures, e.g. FeH_5 at 130 GPa and LaH_{10} at 170 GPa. With the motivation of discovering new hydrogen-rich high- T_c superconductors at lowest possible pressure, here we report the prediction and experimental synthesis of cerium superhydride CeH_9 at 80-100 GPa in the laser-heated diamond anvil cell coupled with synchrotron X-ray diffraction. Ab initio calculations were carried out to evaluate the detailed chemistry of the Ce-H system and to understand the structure, stability and superconductivity of CeH_9 . CeH_9 crystallizes in a $P6_3/mmc$ clathrate structure with a very dense 3-dimensional atomic hydrogen sublattice at 100 GPa. These findings shed a significant light on the search for superhydrides in close similarity with atomic hydrogen within a feasible pressure range. Discovery of superhydride CeH_9 provides a practical platform to further investigate and understand conventional superconductivity in hydrogen rich superhydrides.

¹Center for High Pressure Science & Technology Advanced Research (HPSTAR), 100094 Beijing, China. ²Department of Geosciences, Center for Materials by Design, and Institute for Advanced Computational Science, State University of New York, Stony Brook, New York, NY 11794-2100, USA. ³Institute of Atomic and Molecular Physics, Sichuan University, 610065 Chengdu, China. ⁴Department of Problems of Physics and Energetics, Moscow Institute of Physics and Technology, 9 Institutskiy Lane, Dolgoprudny City, Moscow Region 141700, Russia. ⁵Dukhov Research Institute of Automatics (VNIIA), Moscow 127055, Russia. ⁶Department of Mechanical Engineering, The University of Texas at Austin, Austin, TX 78712, USA. ⁷Center for Advanced Radiation Sources, University of Chicago, Chicago 60637 IL, USA. ⁸Skolkovo Institute of Science and Technology, Skolkovo Innovation Center, 3 Nobel Street, Moscow 143026, Russia. ⁹International Center for Materials Design, Northwestern Polytechnical University, 710072 Xi'an, China. ¹⁰Department of Geological Sciences, The University of Texas at Austin, Austin, TX 78712, USA. *email: artem.oganov@stonybrook.edu; afu@jsg.utexas.edu

Metallization of hydrogen under high pressure has been a topic of great scientific interest in the past few decades mainly due to expectations of room-temperature superconductivity^{1–7}. Hydrogen is expected to become metallic under high pressure above 400 GPa^{7–9}. But achieving such pressures and verifying superconductivity are very challenging in diamond anvil cell (DAC) experiments, mainly due to diamond failure and lack of a reliable probe on the tiny sample volumes at such high pressures. Alternatively, hydrogen-rich hydrides can also be expected to achieve high- T_c superconductivity perhaps at a much lower pressure than that of required for metallic hydrogen^{10–12}. Both hydrides and metallic hydrogen are expected to be conventional superconductors. High phonon frequency, strong electron–phonon coupling, and high density of states at the Fermi level are the essential conditions for superconductivity with Cooper pairs mediated by electron–phonon interaction¹³. Hydrides may satisfy all these conditions as the low mass of hydrogen results in high phonon frequency; covalent bonding is favourable for strong electron–phonon coupling; metallization under high pressure can result in high electronic density of states at the Fermi level¹⁰. Within this view the remarkable prediction and experimental confirmation of superconductivity at a record high T_c of 203 K under pressure of 150 GPa in H_3S makes sense^{14,15}. The discovery of superconductivity in H_3S gave hopes to achieve room-temperature superconductivity in hydrogen-rich systems under high pressure. Recently superconductivity with T_c of 260 K at 180 GPa and 250 K at 170 GPa were reported for LaH_{10} by two different research groups by electrical conductivity measurement^{16,17}. Detecting Meissner effect to confirm the superconductivity has been difficult because signal from extremely small sample could be too weak to be picked up by the state-of-the-art techniques. At such pressure the verification of T_c becomes a challenging task. A recent study by Drozdov et al. reported T_c of 250 K in LaH_{10} , which decreases with the application of magnetic field, and the isotope effect was also observed¹⁷. The discovery of superconductivity in LaH_{10} is a milestone in the search of room temperature superconductivity.

Hydrogen readily reacts with most elements to form binary hydrides^{18,19}. Several hydrogenic motifs such as $H^{\delta-}$, $H_2^{\delta-}$, H_3^- , H_3^+ , H_4^- , and H_5^+ , and infinite chains, layers, frameworks were predicted to occur in high-pressure hydrides^{20–22}. One-dimensional hydrogen chains and three-dimensional clathrate structures with hydrogen cage were predicted and found to be good candidates for high T_c superconductivity²⁰. Recent theoretical predictions have reported several systems with unusually high hydrogen content, termed as polyhydrides/superhydrides, to become stable under high pressure and to exhibit significantly high T_c under pressure^{22–29}. Notably CaH_6 ²⁴, MgH_6 ²⁶, YH_6 ²⁷, YH_9 ²³, YH_{10} ^{23,28}, LaH_{10} ²⁸, ThH_{10} ³⁰, AcH_{10} , and AcH_{16} ²⁹ were predicted to have T_c above 235 K. Most of the phases with T_c close to room temperature are predicted to have a clathrate structure with hydrogen forming a cage around metal atom (M). In MH_6 , MH_9 , and MH_{10} compounds, metal atoms are located within H_{24} , H_{29} , and H_{32} cages, respectively^{23,24,27,28}. However, it is essential to know the experimental pressure–temperature condition to stabilize a hydride before carrying out the further electrical or magnetic measurement to verify the superconductivity. Recently, a handful of experiments were reported to synthesize new superhydrides under pressure, particularly FeH_5 at 130 GPa³¹, LaH_{10} at 170 GPa³², UH_7 , UH_8 , and UH_9 above 37 GPa³³. There were also experimental reports about synthesis of new and unusual hydrides under pressure, such as LiH_6 ³⁴, NaH_7 ³⁵, $Xe(H_2)_7$ ³⁶, and $HI(H_2)_{13}$ ³⁷ with H_2 -like molecular units. Hydrides possessing H_2 -molecular units are not prone to have higher T_c as they tend to have low densities of states at the Fermi level²³. Synthesis of FeH_5 and LaH_{10} without any H_2 -like unit is

very intriguing. Interestingly, FeH_5 crystallized in layered structure consists two-dimensional atomic hydrogen slabs. LaH_{10} has three-dimensional clathrate structure in which La atoms surrounded by hydrogen cage. H_3S has body-centered cubic structure which can also be visualized as sulfur atom surrounded by three-dimensional hydrogen cage. Nearest H–H distance in FeH_5 was reported to be ~ 1.336 Å at ~ 100 GPa³¹, whereas for LaH_{10} it was ~ 1.196 Å at ~ 120 GPa³². LaH_{10} was claimed as a closest analogue to solid atomic metallic hydrogen based on nearest H–H distance³². However, the pressure required to stabilize FeH_5 and LaH_{10} phases was 130 and 170 GPa, respectively^{31,32}. Synthesis of superhydrides at lower pressures would give an opportunity to further investigate superconductivity in these hydrides with a wide range of probes. Studies on the synthesis path and structure of superhydrides also help to build a deeper understanding of hydride chemistry. Besides superconductivity, hydrides are also very important as hydrogen storage materials for next-generation energy-related applications³⁸. Recently, Peng et al.²³ predicted that hydrogen-rich CeH_9 with $P6_3/mmc$ structure becomes stable at a relatively low pressure of 100 GPa, which by itself is very interesting although their estimated superconducting T_c was relatively low, <56 K.

We have carefully studied the Ce–H system in order to understand the crystal chemistry and to seek for superconductivity with, possibly, much higher T_c values. Here we report the successful synthesis of cerium superhydride CeH_9 at 80–100 GPa with laser heating up to ~ 2000 K. Using evolutionary variable-composition searches, the whole compositional space of the Ce–H system explored in a single simulation. We predicted phase stability and superconducting properties of high-pressure cerium superhydrides. Rich chemistry of cerium hydrides manifests itself in numerous stable compounds, including the experimentally synthesized CeH_3 and superhydrides CeH_9 . We have carried out a direct elemental reaction between cerium and hydrogen using a laser-heated DAC coupled with synchrotron X-ray diffraction (XRD). It is found that heating plays an essential role in the formation of Ce–H phases at high pressures. Analysis of XRD results in combination with ab initio calculations shows that CeH_9 crystallizes in a clathrate structure with space group $P6_3/mmc$ at 80–100 GPa after laser heating. Each cerium atom is enclosed within a cage of H_{29} in which hydrogen atoms are bonded covalently. Besides this, a previously unknown $Pm\bar{3}n$ structured CeH_3 (β - UH_3 type³⁹) was synthesized at 36 GPa with laser heating. The detailed first-principles investigation of stability, structural, electronic, and superconducting properties of experimentally synthesized hydrogen-rich phase was carried out. We studied, specifically electron–phonon interaction of $P6_3/mmc$ - CeH_9 and predicted that the CeH_9 is a high temperature superconductor with $T_c = 105$ – 117 K at 200 GPa.

Results

Synthesis of various Ce–H phases. In our experiment, various phases of the Ce–H system such as CeH_x ($x = 2, 2.5, 3$, and 9) were synthesized successfully at high pressures. Initially, the cerium sample and hydrogen gas were loaded into the sample chamber of the DAC and were kept at 9 GPa. A small piece of gold also was loaded along with sample to calibrate pressure. At 9 GPa and ambient temperature, we found that cerium and hydrogen reacted, which resulted in the formation of a cerium hydride compound as shown by the XRD pattern in Fig. 1a. The corresponding XRD image is shown in Supplementary Fig. 1a. All the peaks observed at 9 GPa could be indexed with the $Fm\bar{3}m$ phase of CeH_2 (see Supplementary Note 1). The $Fm\bar{3}m$ phase of CeH_2 persisted up to 33 GPa (Supplementary Fig. 1b). Le Bail refinements were carried to extract lattice parameters of the CeH_2

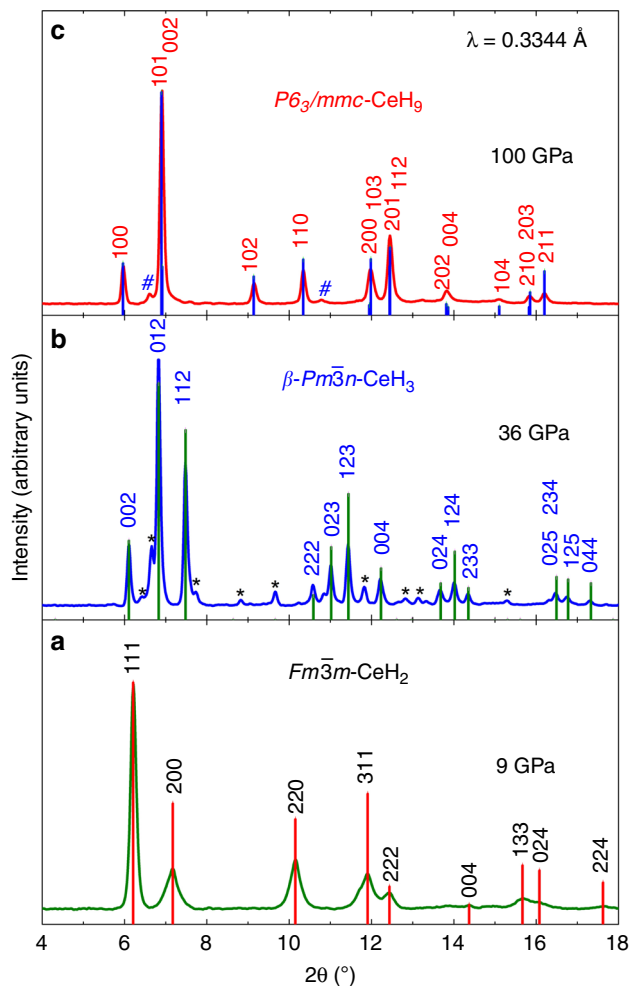


Fig. 1 Representative integrated XRD patterns of high-pressure phases in Ce–H system up to 100 GPa. Typical XRD patterns of **a** CeH₂, **b** CeH₃, and **c** CeH₉ obtained at 9, 36, and 100 GPa of pressure respectively. Vertical lines indicate the indexing with calculated intensity for respective crystal structure. CeH₂, CeH₃, and CeH₉ crystallize in space group $Fm\bar{3}m$, $Pm\bar{3}n$ (β -UH₃ type) and $P6_3/mmc$, respectively. Unidentified weak peaks in **b** and **c** are marked with black asterisk and blue hash symbols, respectively. These additional peaks could not be identified or indexed with any of the known or predicted phases of Ce⁶⁸ or CeH_x²³, as well as cerium oxides^{69,70}

phase (Supplementary Fig. 1c). The lattice parameters of CeH₂ at 9 and 33 GPa were determined as $a = 5.370(1)$ and $a = 5.011(2)$ Å respectively. Pressure dependence of the unit cell volume of CeH₂ was fitted with a third-order Birch–Murnaghan equation of state (EOS) which yielded the fitting parameters such as unit cell volume at zero pressure $V_0 = 44(1)$ Å³ per f.u., bulk modulus $K_0 = 45(6)$ GPa and first pressure derivative of bulk modulus $K_0' = 4$ (fixed) (Supplementary Fig. 1d). Pressurization of CeH₂ up to 33 GPa did not result in any changes in crystal structure. However, microsecond pulsed laser heating of ~2000 K carried at 33 GPa resulted in obvious structural changes (Supplementary Fig. 2a). The XRD pattern at 36 GPa obtained after laser heating is shown in Fig. 1b, and the corresponding XRD image is shown in Supplementary Fig. 2b. The integrated XRD pattern at 36 GPa was found to be of cubic CeH₃ with $Pm\bar{3}n$ isomorphous to β -UH₃ (β - $Pm\bar{3}n$)³⁹. This high-pressure phase of CeH₃ with β - $Pm\bar{3}n$ structure has also been predicted in our evolutionary searches to be the energetically favourable phase below 10 GPa and is 32 meV/atom higher in enthalpy than the most favourable CeH₃

at the synthesized pressure of 36 GPa (Supplementary Fig. 3). However, inclusion of spin–orbit coupling (SOC) and magnetism changes the enthalpy difference of CeH₃ phases by some 0.09 eV per atom. While these calculations affect predicted phase stability range, our experimental results confirm the existence of the predicted phase. To the best of our knowledge, β -UH₃ type $Pm\bar{3}n$ -CeH₃ is being reported for the first time here. The experimental lattice parameters of the β - $Pm\bar{3}n$ phase at 36 GPa are $a = 6.2788(3)$ Å. In β - $Pm\bar{3}n$ structure of CeH₃, cerium atoms occupy 2a (0, 0, 0) and 6c (1/4, 0, 1/2) Wyckoff positions³⁹. Unfortunately, very low X-ray scattering factor of hydrogen atom did not allow us to determine the exact position of hydrogen atoms in CeH₃ unit cell from the experimental XRD data. Theoretical calculations yielded the Wyckoff position for the hydrogen atoms as 24 K (0, 0.1580, 0.6935) at 35 GPa with lattice parameter $a = 6.2471$ Å, which is highly consistent with the experimental value of β - $Pm\bar{3}n$ -CeH₃ observed at 36 GPa. The β - $Pm\bar{3}n$ phase of CeH₃ proved stable with further compression up to 80 GPa and also sustained laser heating at an intermediate pressure of 60 GPa (Supplementary Fig. 2a), which agrees with our predictions. A third-order Birch–Murnaghan EOS was used to fit the P - V data of CeH₃ (see Supplementary Fig. 2d), fitting parameters are $V_0 = 39.7(4)$ Å³ per f.u., $K_0 = 86(4)$ GPa and $K_0' = 4$ (fixed).

Several cycles of pulse laser heating with 1 μ s pulse width at a repetition rate of 10 kHz for a total heating duration of a few seconds each cycle was used to laser heat the sample assemblage to approximately 1700 K at 80 GPa that resulted in the emergence of new peaks (Supplementary Fig. 4). These new diffraction peaks were indexed to be (101) and (002) of clathrate hexagonal phase of CeH₉ (Figs. 1c and 2, also see in Supplementary Fig. 4) as found by our evolutionary search. With further pressurization the relative intensity of the (101) and (002) peaks of CeH₉ phase increased (Supplementary Fig. 4). Although most of the peaks of CeH₃ phase were present, the intensity of the CeH₉ peaks became prominent and increased with pressure (Supplementary Fig. 4). Several further cycles of laser heating at 88 GPa (Supplementary Fig. 4) and 98 GPa improved the intensity of the hexagonal CeH₉ phase, as shown in Fig. 1c. A Rietveld refinement plot for the CeH₉ phase at 100 GPa is shown in Fig. 2a with the corresponding XRD image as an inset. CeH₉ crystallizes in the $P6_3/mmc$ space group with lattice parameters $a = 3.7110(3)$ and $c = 5.5429(7)$ Å at 100 GPa. Cerium atoms occupy the Wyckoff position 2d (2/3, 1/3, 1/4) in a hexagonal unit cell. Theoretical calculations established positions of hydrogens to be 2b (0, 0, 1/4), 4f (1/3, 2/3, 0.1499), and 12k (0.1565, 0.8435, 0.4404) at 100 GPa. The crystal structure of CeH₉ is shown in Fig. 2b. The experimentally observed $P6_3/mmc$ CeH₉ phase and its structural parameters are perfectly consistent with our calculations. Calculated EOS parameters for CeH₉ phase are $V_0 = 53.4(2)$ Å³ per f.u., $K_0 = 80.5(13)$ GPa and $K_0' = 4$ (fixed). Synthesis of the $P6_3/mmc$ -CeH₉ phase has been confirmed in two independent experimental runs.

During the decompression cycle, the CeH₉ phase was observed to start to become unstable at pressures below 93 GPa and ambient temperature (supplementary Fig. 5). Laser heating was also carried out during the decompression cycle at 79 and 54 GPa. Laser heating in decompression cycle did not result in any changes in XRD pattern. Upon further decompression, the β - $Pm\bar{3}n$ -CeH₃ phase reappeared below 50 GPa (supplementary Fig. 5). Finally, after complete decompression, the β - $Pm\bar{3}n$ -CeH₃ phase was recovered at ambient conditions along with tetragonal Ce₂H₅ (Supplementary Fig. 5). The P - T path for the formation and stability of various Ce–H phases, observed in our experiments, can be seen in Fig. 3. All these findings are repeatable as demonstrated in a separate run of experiment (see Supplementary Note 2 and Supplementary Fig. 6).

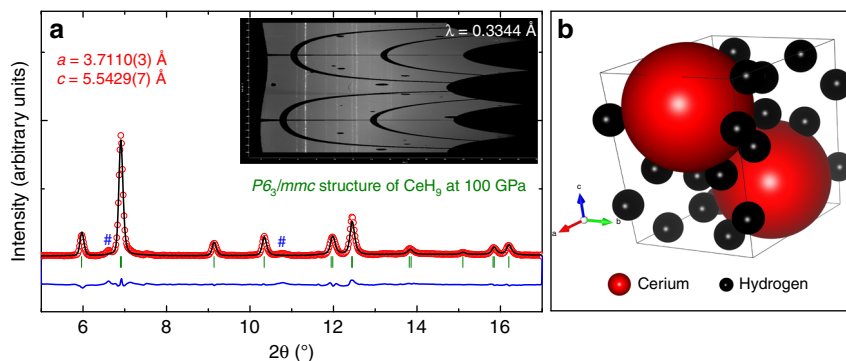


Fig. 2 XRD pattern and the result of Rietveld refinement for the hexagonal CeH_9 in $P6_3/mmc$ structure. **a** Rietveld refinement plot of powder XRD data at 100 GPa. Red open circles: experimental data of CeH_9 in $P6_3/mmc$ structure at 100 GPa; black line: simulated XRD based on the structural model; green vertical lines: Bragg diffraction positions of the structure; blue line: the difference between the simulated and the original XRD. Reliability parameters for the Rietveld refinement are as follows (in %): $R_p = 14.5$, $R_{wp} = 18.4$, $R_{\text{Bragg}} = 8.05$. Blue hash symbols represent unidentified weak peaks. Inset shows the Pilatus XRD image of corresponding powder XRD pattern with the incident X-ray wavelength of 0.3344 Å. **b** Crystal structure model of $P6_3/mmc$ structured CeH_9 . Red and black spheres represent cerium and hydrogen atoms, respectively

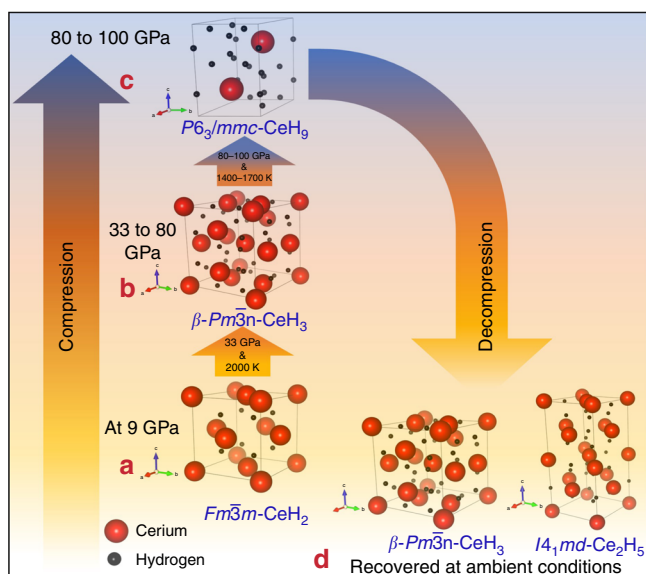


Fig. 3 Pressure temperature path for the synthesis and stability of various Ce-H phases. **a** Starting at 9 GPa, cerium reacts with hydrogen to form $Fm\bar{3}m\text{-CeH}_2$, which remained stable up to 33 GPa. **b** At 33 GPa with laser heating, $Fm\bar{3}m\text{-CeH}_2$ in H_2 medium reacted to form $\beta\text{-Pm}\bar{3}n\text{-CeH}_3$. $\beta\text{-Pm}\bar{3}n\text{-CeH}_3$ remained stable up to 80 GPa. **c** Laser heating of $\beta\text{-Pm}\bar{3}n\text{-CeH}_3$ in H_2 medium at 80–100 GPa resulted in the occurrence of the $P6_3/mmc\text{-CeH}_9$ superhydride. The superhydride phase was found to be stable up to the maximum pressure reached in our studies i.e. 100 GPa. **d** After complete decompression, $\beta\text{-Pm}\bar{3}n\text{-CeH}_3$ and $I4_1md\text{-Ce}_2\text{H}_5$ were recovered at ambient conditions

Theoretical calculations and prediction of cerium hydrides.

First-principles calculations were carried out to understand the detailed chemistry of the Ce–H system, dynamical stability, and structural and electronic band structures of experimentally synthesized superhydride phases. We performed variable-composition evolutionary searches at 0, 50, 100, 150, 200, and 250 GPa. The thermodynamic convex hull at different pressures is depicted in Fig. 4. The predicted stable cerium hydrides are shown in the pressure–composition phase diagram in Fig. 5. Several compounds such as $I4/mmm\text{-CeH}_4$, $P6_3mc\text{-CeH}_6$, $P6_3mc\text{-CeH}_8$, $P6_3/mmc\text{-CeH}_9$, and $Fm\bar{3}m\text{-CeH}_{10}$, were predicted, in addition to finding three known compounds CeH_2 , Ce_2H_5 , and CeH_3 . High-pressure phase of the CeH_3 was also predicted with

space group $Pm\bar{3}n$, as shown in Fig. 5. Because of high concentration of hydrogen in hydrogen-rich hydrides, zero-point energy (ZPE) might be important in determining the relative stability of hydrogen-rich phases; however, in our previous studies^{22,40}, we showed that this quantum effect does not change the topology of the phase diagram, and quantitative effects are just moderate shifts in transition pressures. For example, for GeH_4 the inclusion of ZPE shifts the transition pressure $Ama2 \rightarrow C2/m$ from 300 to 278 GPa⁴⁰. Among the stable phases predicted, we have synthesized $Fm\bar{3}m\text{-CeH}_2$, $I4_1md\text{-Ce}_2\text{H}_5$, $\beta\text{-Pm}\bar{3}n\text{-CeH}_3$, and $P6_3/mmc\text{-CeH}_9$. Our pressure–composition phase diagram shows pressure ranges of stability for all the predicted phases along with experimentally known compounds. It clearly shows that higher pressures favour higher hydrogen content compounds, which is consistent with our experiment done at different pressure conditions. Previously known compounds $Fm\bar{3}m\text{-CeH}_2$ and $I4_1md\text{-Ce}_2\text{H}_5$ are predicted to be stable only below 8 and 1.5 GPa, respectively. Increase of pressure leads to the formation of $I4/mmm\text{-CeH}_4$ above 32 GPa. CeH_6 and CeH_8 are stable in relatively narrow pressure ranges from 26 to 68 GPa, and 55 to 95 GPa, respectively and that is probably why they are not observed in our experiment. $P6_3/mmc\text{-CeH}_9$ becomes stable at pressures above 78 GPa, which agrees with our high-pressure experiments where it was synthesized at 80–100 GPa after laser heating. Detailed structural information on the predicted phases can be found in Supplementary Table 1. Among the predicted stable cerium hydrides, we focus on modelling of hydrogen-rich CeH_9 , since a higher hydrogen to metal ratio in hydrides is expected to correlate with higher T_c superconductivity in hydrogen-rich hydrides¹¹.

Discussion

Addition of hydrogen in metallic sublattice expands the unit cell volume. In most cases, an increase in volume is proportional to hydrogen content in hydride. In hydrides, expansion of the cell volume with respect to pure metal volume was frequently used to establish the hydrogen content and stoichiometry³². In order to ascertain the stoichiometry of high pressure superhydride phase observed at 80–100 GPa after laser heating, we have compared the ideal mixture of Ce– H_2 solution with experimental volume per formula unit of CeH_3 , CeH_9 , and with theoretical EOS (see Fig. 6a). The curve representing ideal mixture of Ce and (7/2) H_2 lies well below the theoretical and experimental EOS of $P6_3/mmc\text{-CeH}_9$ in the pressure range 80–100 GPa, whereas mixture of Ce and (8/2) H_2 partially overlaps with theoretical and experimental

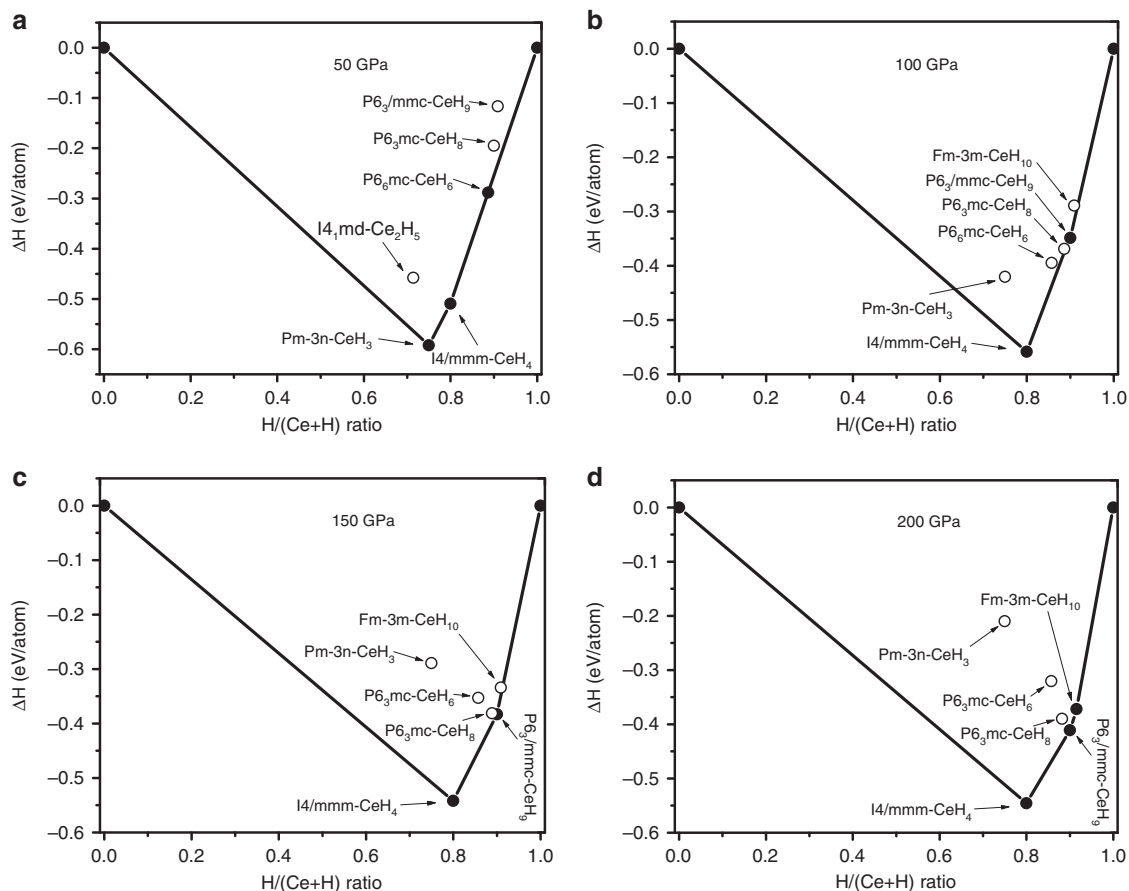


Fig. 4 Convex hull diagram of Ce-H system. Predicted formation enthalpy of $Ce_{1-x}H_x$ as a function of H concentration at selected pressures. Open circles above the convex hull show unstable compounds with respect to decomposition into the two adjacent phases on the convex hull, while solid circles show thermodynamically stable compounds

EOS of CeH_9 . This indicates that the hexagonal phase observed at 80-100 GPa after laser heating does not favour energetically CeH_x with $x < 8$ and can decompose into its elemental constituents or hydride with $x > 8$ and hydrogen. On the other hand, the curve representing an ideal mixture of Ce and $(9/2) H_2$ lies well above the theoretical and experimental EOS of CeH_9 in the pressure range 80-100 GPa. This observation clearly indicated that CeH_9 can be stabilized in the pressure range mentioned. From our theoretical calculations and energetic considerations, it clearly signifies that the hexagonal phase observed at 80-100 GPa with laser heating has the CeH_9 stoichiometry. We can also see that there is a fair agreement between experimental volume and theoretical EOS results (Fig. 6a) for $P6_3/mmc-CeH_9$ as well as $\beta-Pm\bar{3}n-CeH_3$.

In hydrides, hydrogen is pre-compressed by interaction with metal atoms. Hydrogen sublattice in hydrides might be expected to be identical with atomic metallic hydrogen. So, we compared the volume expansion (ΔV_H) per hydrogen atom and nearest H-H distance in CeH_9 with simulated atomic metallic hydrogen phase extrapolated to lower pressure³¹ and also with other reported hydrides as shown in Fig. 6b, c, respectively^{31,32,41,42}. The nearest Ce-H distance in $P6_3/mmc-CeH_9$ is plotted in Fig. 6d. The inset of Fig. 6d shows the Ce- H_{29} clathrate cage structure in which the H_{29} cage is encapsulating a cerium atom. ΔV_H per H atom for CeH_9 is 2.09 \AA^3 at 100 GPa, which is lower than that for a hydrogen atom, but larger by ~8% with respect to ΔV_H per H atom of layered FeH_5 . ΔV_H per H atom for CeH_9 matches with volume of atomic metallic hydrogen around 100 GPa. Formation of CeH_9 can also be understood in terms of

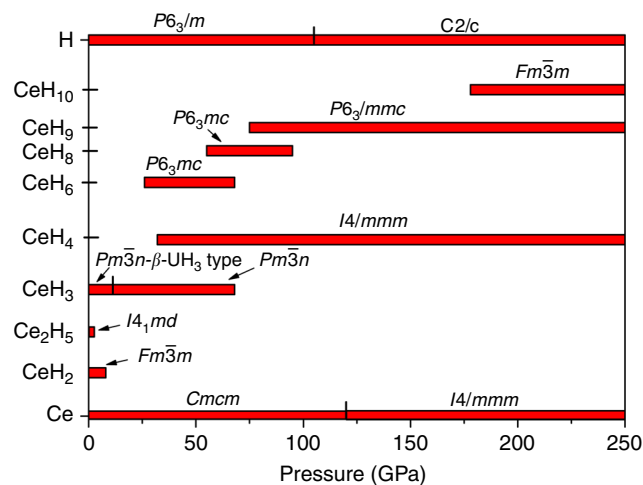


Fig. 5 Pressure-composition phase diagram of theoretically predicted stable phases in the Ce-H system at high pressures. Red horizontal bars show the range of stability of each phase; this phase diagram was created on the basis of the evolutionary structure prediction method USPEX. The experimentally discovered $P6_3/mmc-CeH_9$ is predicted to be stable from 78 GPa up to at least 250 GPa.

mixing of Ce and dense atomic metallic hydrogen. This indicates that hydrogen framework surrounding Ce atom is identical to dense atomic metallic hydrogen at a lower pressure. Nearest H-H distance in clathrate CeH_9 is 1.116 \AA at 100 GPa, which is

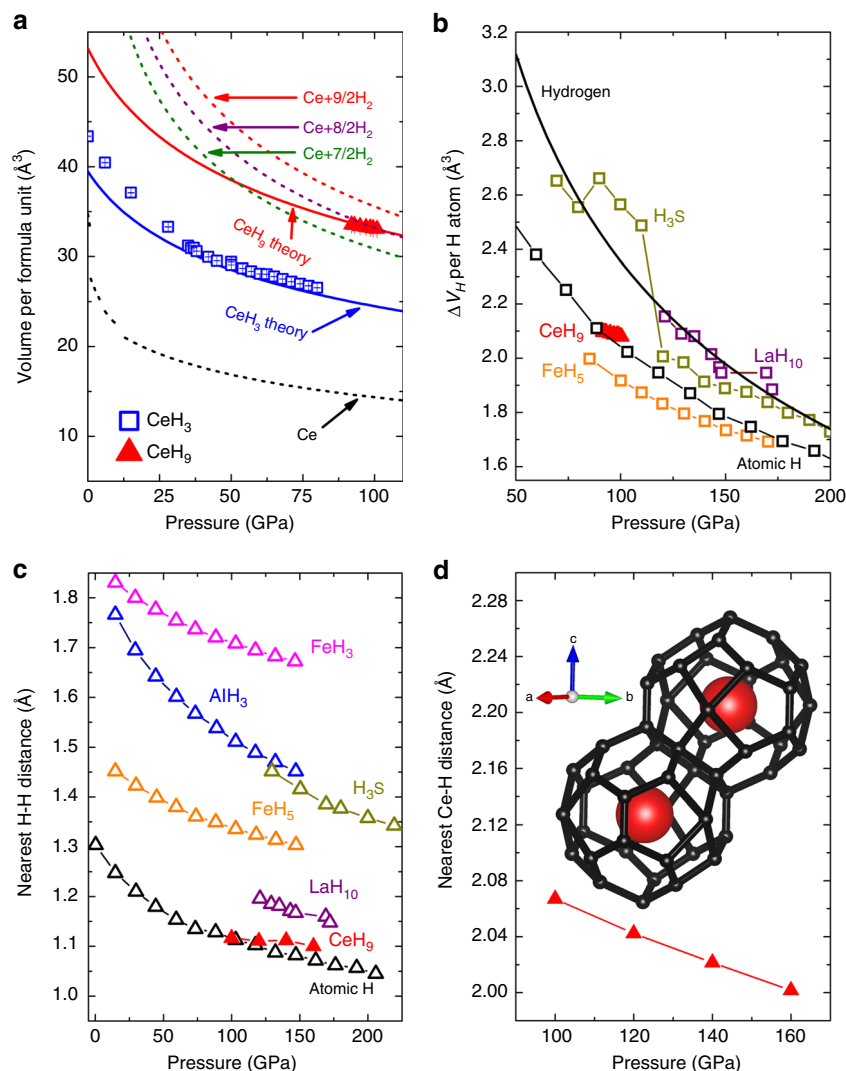


Fig. 6 Effect of hydrogen on unit cell volume and nearest neighbour distances in various hydrides at different pressures. **a** Experimentally obtained volume per formula unit for CeH_3 and CeH_9 plotted as a function of pressure. Blue open squares and red solid triangles represent experimental data for CeH_3 and CeH_9 respectively. Errors in the fitting are also plotted. Theoretical EOS of CeH_3 and CeH_9 is plotted as blue and red lines, respectively. Black dashed line represents EOS of cerium metal⁶⁸. Red, purple and green dashed curves represent ideal mixtures of $\text{Ce}+(9/2)\text{H}_2$, $\text{Ce}+(8/2)\text{H}_2$, and $\text{Ce}+(7/2)\text{H}_2$, respectively^{68,71}. **b** Volume expansion (ΔV_{H}) per hydrogen atom plotted against pressure for CeH_9 , FeH_5 ³¹, H_3S ¹⁴, LaH_{10} ³², H ⁷¹, and atomic H ³¹ for comparison. Dark yellow, purple, black, and orange open triangle symbol-line represents H_3S , LaH_{10} , atomic H , and FeH_5 , respectively. Red solid triangle symbols represent CeH_9 . Black solid line represents hydrogen. **c** Comparison of the pressure dependence of the nearest H–H distances for CeH_9 , FeH_3 ⁴¹, FeH_5 ³¹, AlH_3 ⁴², H_3S ¹⁴, LaH_{10} ³², and atomic H ³¹. Magenta, blue, dark yellow, orange, purple, and black open triangle symbol line represents FeH_3 , AlH_3 , H_3S , FeH_5 , LaH_{10} , and atomic H , respectively. Red solid triangle symbol line represents CeH_9 . **d** Nearest Ce–H distance for CeH_9 as a function of pressure. Inset shows CeH_{29} clathrate cage in $P6_3/mmc$ structure. [Pressure-dependent experimental data is at 300 K, whereas theoretical data is at 0 K]

significantly longer than the H–H bond length (0.74 \AA) in H_2 gas molecules but is significantly lower than other hydrides such as AlH_3 , FeH_3 , FeH_5 , H_3S , and LaH_{10} as can be seen in Fig. 6c. Surprisingly, the nearest H–H distance in CeH_9 almost overlaps with the H–H distance in atomic hydrogen and decreases very slowly with pressure. Among all the superhydrides, the nearest H–H distance observed in CeH_9 is among the shortest at 100 GPa and coincides with H–H distance of atomic metallic hydrogen. Among the reported hydrides, nearest H–H distance of CeH_9 is only second to the H–H distance (0.98 \AA)²³ for atomic metallic hydrogen at 500 GPa at which hydrogen is in a superconducting metallic state⁴³. Judging from the H–H distances, CeH_9 is closer to monatomic metallic hydrogen than other hydrides, yet its predicted T_c is not as high as that of hydrogen or of LaH_{10} . The shortest H–H distance is not the only thing that

matters for high T_c ; the electronic structure of the metal atom plays a crucial role, as shown by Semenov et al.²⁹. In Fig. 6c, we can also see that non-superconducting FeH_5 has shorter H–H distance than H_3S compound well known for very high T_c . Presence of strongly coupled hydrogen-dominant libration and stretch vibrations are the signatures of high- T_c in hydrogen-rich materials⁴⁴. Weak H–H interactions with preferred bond distances between 1.2 and 1.3 \AA , the stretching and bending vibrations becomes indistinguishable, due to which all H vibrations contribute in the strong electron–phonon coupling process, eventually contributing to enhance the T_c in hydrides⁴⁴. At 100 GPa the nearest Ce–H distance is $\sim 2.07 \text{ \AA}$ and it decreases with pressure. It is noteworthy that the clathrate structures predicted in the literature for rare earth (RE) hydrides REH_6 , REH_9 , and REH_{10} have H_{24} , H_{29} , and H_{30} cages surrounding the RE

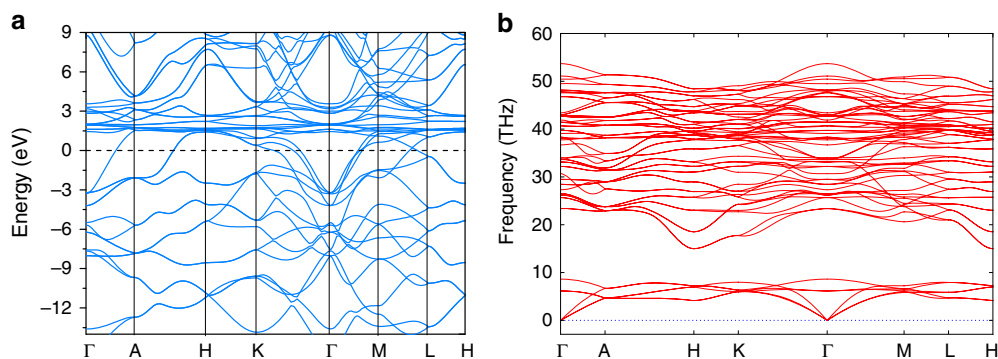


Fig. 7 Electronic band structure and phonon dispersion curves for $P6_3/mmc$ -CeH₉ at 150 GPa. **a** Electronic band structure for $P6_3/mmc$ -CeH₉ at 150 GPa. Dotted line indicates Fermi level. **b** Phonon dispersion curves for $P6_3/mmc$ -CeH₉ at 150 GPa. Absence of imaginary phonons in the dispersion curves shows the dynamical stability of $P6_3/mmc$ -CeH₉ at 150 GPa. Phonon instability at 120 GPa is shown in Supplementary Fig. 8

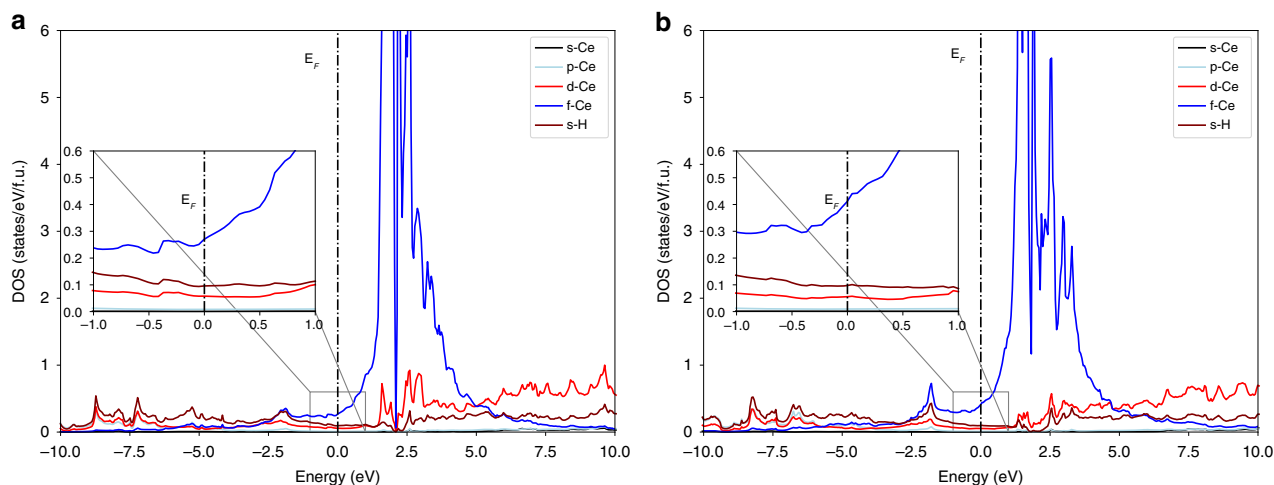


Fig. 8 Electron density of states (DOS) for CeH₉ at 150 GPa. **a** and **b** represents electron DOS computed with and without Hubbard correction respectively. Electron DOS at the Fermi level is largely dominated by Ce-4f and H orbitals

atom²³. Among these cages, The H₂₉ cage has the smallest volume per formula unit for YH₉ (ref. ²³). Clathrate H₂₉ cage in CeH₉ surrounding the Ce atom is almost 1.1 Å thick along the *a*- and *b*-axis, while it is 0.9 Å thick along *c*- axis at 100 GPa⁴⁵, whereas thickness of clathrate cage in LaH₁₀ is 0.9 Å³². Clathrate CeH₉ can be visualized as three-dimensional atomic metallic hydrogen encapsulating Ce atoms (inset of Fig. 6d). Covalently bonded hydrogen sublattice in CeH₉ with bond length and ΔV_H per H atom similar to atomic metallic hydrogen is likely to have density similar to that for atomic hydrogen slab at 100 GPa. Hence $P6_3/mmc$ -CeH₉ will be a good platform to investigate H-H properties to understand atomic metallic hydrogen. Recently, Carbotte et al. proposed a new technique to investigate superconductivity in high pressure hydrides and hydrogen based on optical properties, without four probes⁴⁶. Superconductivity in $P6_3/mmc$ -CeH₉ can also be evaluated using this optical technique.

Figure 7a shows calculated electronic band structures of CeH₉ at 150 GPa. From Fig. 7a, it can be seen that CeH₉ is metallic and features numerous flat bands above the Fermi level. Noticeable density of electronic states at the Fermi level 0.73 (0.62) states per eV per f.u., which is 1.4 (1.2) times higher than that of previously found H₃S¹⁴ and comparable to that of recently synthesized LaH₁₀³² at an optimal pressure of 200 GPa, is a good sign for facilitating high-temperature superconductivity (values in parentheses are the corrected ones using GGA+U with U = 6 eV, see supplementary Table 2). Figure 8a, b represents the electron

density of states (DOS) for CeH₉ at 150 GPa with and without Hubbard correction respectively. The main contributors to $N(E_f)$ are Ce-4f and H-1s orbitals, however, only those electrons that are coupled strongly to phonons are important. High frequency phonons are mainly related to H vibrations, owing to its light mass, which makes the largest contribution to the electron-phonon coupling constant. Analysis of electron localization function (ELF) shows a moderate ELF value 0.64 between H atoms within the unit, suggesting weak covalent interaction, which forms a three-dimensional hydrogen network i.e., H₂₉ cage consisting of H₄, H₅ and H₆ rings. Very low ELF value between Ce and H indicates that no bonds were present between the Ce and H atoms (Supplementary Fig. 7).

We performed phonon calculations in the thermodynamic stability range of CeH₉ i.e., above 80 GPa. Lattice dynamics calculations indicate that the $P6_3/mmc$ -CeH₉ phase is dynamically stable at 150 GPa (Fig. 7b). Selected vibrational mode displacements of the $P6_3/mmc$ -CeH₉ at the H- and K-point from the structure relaxed at 150 GPa are shown in the Supplementary Fig. 8. However, at lower pressures, e.g., 120 GPa and below, DFT calculations show that some phonon modes become imaginary along the H- and K-points ($[-1/3, 2/3, 1/2]$ and $[-1/3, 2/3, 0]$, respectively) (Supplementary Fig. 8). The $P6_3/mmc$ -CeH₉ phase is stabilized anharmonically. To include temperature effect, capturing anharmonicity, we used the approach of Hellman et al.^{47,48}, to obtain temperature-dependent phonon frequencies and the phonon spectra show dynamical stability already at

100 GPa and 500 K (see Supplementary Fig. 9). To resolve the soft modes of the lattice within the harmonic approximation, we used generalized evolutionary metadynamics (GEM)⁴⁹, in which large displacements along the softest mode eigenvectors are used to equilibrate the system. This hybrid technique is implemented in USPEX and was successfully applied to boron and silicon and found numerous energetically competitive configurations⁴⁹. We used supercells up to index 4, i.e., 80 atoms per cell. Using GEM, we found a stable structure within harmonic approximation with $C2/c$ symmetry (Supplementary Fig. 10), which is a subgroup of $P6_3/mmc$ symmetry. Electron–phonon coupling (EPC) calculations revealed that $P6_3/mmc$ -CeH₉ is a high-temperature superconductor. Using the Allen-Dynes modified McMillan equation (Eq. 1), we estimated the superconducting transition temperature (T_c) to be 105–117 K at 200 GPa, when using different Coulomb pseudopotentials (μ^*), i.e., 0.10 and 0.15 which are widely accepted lower and upper bound values. In $P6_3/mmc$, the resulting electron–phonon coupling coefficient λ is 2.30 at 200 GPa, which is higher than that of H₃S, $\lambda = 2.19$ at 200 GPa¹⁴. Since cerium atom is heavy, the logarithmic average phonon frequency ($\omega_{\log} = 740$ K) is lower compared with that of H₃S ($\omega_{\log} = 1335$ K), which results in a lower T_c of 105–117 K. The T_c of CeH₉ has a lower value of 63–75 K at 100 GPa for $C2/c$ structure. The logarithmic average phonon frequency ω_{\log} of the $C2/c$ phase has a lower value 662 K. However, our results indicate that lower T_c value is mainly related to the lower electron–phonon coupling coefficient $\lambda = 1.48$. Earlier report by Peng et al.²³ predicted a slightly lower T_c value of 56 K at 100 GPa for the CeH₉ phase with $P6_3/mmc$ structure²³. However, our phonon calculations within harmonic approximation indicate instability of $P6_3/mmc$ phase below 120 GPa (see Supplementary Fig. 8), and it is unclear how T_c of a dynamically unstable phase was computed. So, our systematically carried studies estimate comparatively higher T_c of 63–75 K for the CeH₉ at 100 GPa for the dynamically stable $C2/c$ structure. Furthermore, we have tabulated the ω_{\log} , λ , and T_c value of CeH₉ along with recently predicted other superhydrides of La-H, Y-H, U-H, Ac-H, and Th-H system for comparison, as shown in Supplementary Table 3. Phonon dispersions curves, phonon density of states, the Eliashberg spectral function $\alpha^2F(\omega)$, and the EPC parameter λ as a function of frequency are calculated and shown in Supplementary Figs. 11 and 12 for $C2/c$ and $P6_3/mmc$ -CeH₉ at 100 and 200 GPa, respectively. It is known that quantum effects can impact the calculated superconducting transition temperatures; however, in the case of strongly anharmonic H₃S (SG $Im\bar{3}m$), the inclusion of anharmonic correction, lowered the T_c from its harmonic 204 K value¹⁴ only to 194 K⁵⁰ at 200 GPa, and both are close to the reported experiment T_c at 200 GPa¹⁵, although the transition pressures shift is considerably large^{14,51}.

In summary, we have successfully synthesized a cerium superhydride phase of CeH₉ at 80–100 GPa after laser heating, which crystallized in the hexagonal $P6_3/mmc$ clathrate structure. In addition to this we have also synthesized a cubic phase of CeH₃ with space group $Pm\bar{3}n$ (β -UH₃ type), which was recovered at ambient phase after complete decompression. Our studies give strong evidence for the synthesis of rare earth superhydrides and pave the way for future studies on other rare earth-hydrogen systems under extreme pressure with the aid of laser heating perhaps to make the binary hydrides MH_{*x*} with $x > 9$. Apart from this, the estimated T_c of 105–117 K in $P6_3/mmc$ -CeH₉ at 200 GPa is very promising. Electron–phonon coupling in $P6_3/mmc$ -CeH₉ is even higher than in H₃S but still could not achieve higher T_c due to lower logarithmic average phonon frequency. Conspicuously, the dense three-dimensional atomic hydrogen sublattice is noted for superhydride $P6_3/mmc$ -CeH₉ as compared with reported super/polyhydrides and similar to atomic metallic

hydrogen at 100 GPa. The discovery of CeH₉ at a feasible pressure range with prediction of superconductivity will certainly inspire further studies on superconductivity in hydride systems.

Methods

Experimental details. High pressure–temperature (P – T) experiments were carried out using a single-sided laser-heated DAC with a pair of bevelled diamond anvils of size 100–300 μm culets. Polycrystalline cerium (*Alfa Aesar*, 99.9% purity) sample of ~ 5 μm thickness was loaded inside a sample chamber drilled to a diameter of 75 μm in a rhenium gasket of 250 μm initial thickness pre-indented to 18 μm . Cerium is very likely to oxidize in open air so the sample was loaded in an argon filled glove box where both H₂O and O₂ concentrations were maintained below 0.1 ppm. A small piece of gold (~ 5 μm width) was also placed near the sample for pressure calibration as shown in Supplementary Fig. 13. For hydrogen loading, sample chamber was initially sealed by slightly closing the gasket and then opened in the high-pressure gas loading system in order to fill it with high purity hydrogen gas at room temperature under ~ 1.7 kilobar pressure. After hydrogen loading, Raman spectra of the H₂ vibron, collected at 9 GPa from the sample chamber, confirmed the presence of H₂ inside the sample chamber (Supplementary Fig. 14). XRD patterns were recorded at beamline 13-ID-D of GSECARS at the Advanced Photon Source. Angle-dispersive XRD patterns were recorded on a PILATUS CdTe 1M detector with a synchrotron radiation of incident wavelength 0.3344 Å focused to a spot size of $\sim 3 \times 4$ μm (FWHM). A clean-up slit with an 8 μm size pin-hole was used to cut down the beam tails and collect the XRD from the smallest area possible. Pulsed-laser heating was carried out using the online infrared laser set-up with a wavelength of 1064 nm available at beamline 13-ID-D⁵². Several cycles of laser heating were carried at each pressure of 33, 60, 80, 89, 98, and 100 GPa during compression and at 79 and 54 GPa during the decompression run. The use of the pulse laser heating not just helped to promote reaction between Ce and H₂ to form cerium hydrides but also reduced the possibility of diamond anvil failure. Pulsed-laser heating with microsecond pulse width has been utilized to reach temperatures of 1000–2000 K. Every laser heating shot was formed by accumulating 300k frequency modulated laser pulses of one microsecond pulse width at a rate of 10 kHz. The flat top of the laser heating spot size was around 10 μm in diameter. We strictly avoided temperatures above 2000 K to protect diamonds as hydrogen loaded DACs at high P – T conditions are most likely to fail^{35,53}. Maintaining the sample temperature below 2000 K and relatively cold surrounding area using pulsed heating mode helped to avoid contamination and parasitic reaction with the sample chamber wall of gasket. Also, the laser heating spot on the sample was consistently maintained at substantial distance from gasket wall to avoid any contamination due to unwanted reaction (see Supplementary Fig. 15). In situ temperature measurements were carried by fitting the slope of thermal radiation spectra to a Planck radiation function. Uncertainty in temperature measurements were less than ± 100 K. Obtained raw images of XRD were integrated with DIOPTAS software⁵⁴. Rietveld and Le Bail refinements were carried out using FullPROF software.

Computational details. Evolutionary variable-composition simulation, implemented in USPEX, is used to explore the high-pressure phase diagram of the Ce–H system from ambient pressure to 250 GPa. The evolutionary algorithm USPEX^{55–59} is a powerful method for finding thermodynamically stable compounds of a given system and their most stable structures. This method has been shown to be successful in predicting high-pressure structures of variety of systems which were confirmed experimentally, also in a number of specific superconducting hydrides, e.g., UH₈³³ and H₃S¹⁴. In this method, the first generation of structures (100 structures) and compositions are created using the random symmetric algorithm. Subsequent generations were obtained using 40% heredity, 20% transmutation, 20% softmutation, and 20% random symmetric generator. We allowed variation operators to automatically evolve in the subsequent generations. The underlying structure relaxations were carried out using the VASP package⁵⁹ in the framework of DFT and using PBE-GGA (Perdew–Burke–Ernzerhof generalized gradient approximation)^{60,61}. We believe PBE is the most appropriate choice, because PBE best reproduces the experimental data (see Supplementary Fig. 16 and Supplementary Tables 4 and 5). The projector-augmented wave approach (PAW)^{59,62} was used to describe the core electrons and their effects on valence orbitals. Valence electron configuration of $5s^2 5p^6 4f^1 5d^1 6s^2$ (i.e., with explicitly included f electrons) and $1s^1$ was used for the Ce and H atoms, respectively. A plane-wave kinetic-energy cut-off of 1000 eV for hard PAW potentials and dense Monkhorst–Pack k -points grids with reciprocal space resolution of $2\pi \times 0.03 \text{ \AA}^{-1}$ were employed⁶³ to sample the Brillouin zone. Phonon frequencies and superconducting critical temperature were calculated using density-functional perturbation theory as implemented in the QUANTUM ESPRESSO package⁶⁴, also using the PBE-GGA functional. Ultrasoft pseudopotentials for Ce and H were used with a plane-wave basis set cut-off of 70 Ry, which gives a convergence in energy with a precision of 1 meV per atom. Phonon dispersions were also calculated under the quasi-harmonic approximation using the finite displacement method implemented in PHONOPY package⁶⁵ using forces computed with VASP. The k -space integration (electrons) was approximated by a summation over a $12 \times 12 \times 6$ uniform grid in reciprocal space, with the smearing scheme of Methfessel–Paxton and a fictitious smearing temperature T of $k_B T = 0.05$ Ry for self-consistent cycles and

relaxations; a much finer ($24 \times 24 \times 12$) grid was used for evaluating DOS and electron–phonon linewidths. Dynamical matrices and electron–phonon linewidths of $P6_3/mmc$ -CeH₉ were calculated on a uniform $6 \times 6 \times 3$ grid in q-space. Electron–phonon matrix elements were calculated based on interpolation method developed by Wierzbowska et al.⁶⁶. The superconducting transition temperature T_c was estimated using the Allen–Dynes modified McMillan equation⁶⁷

$$T_c = \frac{\omega_{\log}}{1.2} \exp\left(\frac{-1.04(1 + \lambda)}{\lambda - \mu^*(1 + 0.62\lambda)}\right), \quad (1)$$

where μ^* is the Coulomb pseudopotential and ω_{\log} is the logarithmic average phonon frequency. The electron–phonon coupling constant λ and ω_{\log} were calculated as

$$\omega_{\log} = \exp\left(\frac{2}{\lambda} \int \frac{d\omega}{\omega} \alpha^2 F(\omega) \ln(\omega)\right), \quad (2)$$

$$\lambda = 2 \int_0^{\infty} \frac{\alpha^2 F(\omega)}{\omega} d\omega. \quad (3)$$

Data availability

All data supporting the findings of this study are included in this article and its Supplementary Information, and are also available from the corresponding authors upon request. Data are deposited on <https://figshare.com/> and can be found on the link—<https://doi.org/10.6084/m9.figshare.9729467.v3>

Received: 14 March 2019; Accepted: 28 August 2019;

Published online: 01 October 2019

References

- Wigner, E. & Huntington, H. B. On the possibility of a metallic modification of hydrogen. *J. Chem. Phys.* **3**, 764–770 (1935).
- Ashcroft, N. W. Metallic hydrogen: a high-temperature superconductor? *Phys. Rev. Lett.* **21**, 1748–1749 (1968).
- Loubeyre, P., Occelli, F. & LeToullec, R. Optical studies of solid hydrogen to 320 GPa and evidence for black hydrogen. *Nature* **416**, 613 (2002).
- Eremets, M. I. & Troyan, I. A. Conductive dense hydrogen. *Nat. Mater.* **10**, 927 (2011).
- Dalladay-Simpson, P., Howie, R. T. & Gregoryanz, E. Evidence for a new phase of dense hydrogen above 325 gigapascals. *Nature* **529**, 63 (2016).
- Dias, R. P. & Silvera, I. F. Observation of the Wigner-Huntington transition to metallic hydrogen. *Science* **355**, 715 (2017).
- Borinaga, M., Errea, I., Calandra, M., Mauri, F. & Bergara, A. Anharmonic effects in atomic hydrogen: superconductivity and lattice dynamical stability. *Phys. Rev. B* **93**, 174308 (2016).
- Azadi, S., Monserrat, B., Foulkes, W. M. C. & Needs, R. J. Dissociation of high-pressure solid molecular hydrogen: a quantum Monte Carlo and Anharmonic vibrational study. *Phys. Rev. Lett.* **112**, 165501 (2014).
- McMinis, J., Clay, R. C., Lee, D. & Morales, M. A. Molecular to atomic phase transition in hydrogen under high pressure. *Phys. Rev. Lett.* **114**, 105305 (2015).
- Gor'kov, L. P. & Kresin, V. Z. Colloquium: high pressure and road to room temperature superconductivity. *Rev. Mod. Phys.* **90**, 011001 (2018).
- Ashcroft, N. W. Hydrogen dominant metallic alloys: high temperature superconductors? *Phys. Rev. Lett.* **92**, 187002 (2004).
- Struzhkin, V. V. Superconductivity in compressed hydrogen-rich materials: pressing on hydrogen. *Physica C* **514**, 77–85 (2015).
- McMahon, J. M. & Ceperley, D. M. High-temperature superconductivity in atomic metallic hydrogen. *Phys. Rev. B* **84**, 144515 (2011).
- Duan, D. et al. Pressure-induced metallization of dense (H₂S)₂H₂ with high-T_c superconductivity. *Sci. Rep.* **4**, 6968 (2014).
- Drozdov, A. P., Eremets, M. I., Troyan, I. A., Ksenofontov, V. & Shylin, S. I. Conventional superconductivity at 203 kelvin at high pressures in the sulfur hydride system. *Nature* **525**, 73 (2015).
- Somayazulu, M. et al. Evidence for superconductivity above 260 K in lanthanum superhydride at megabar pressures. *Phys. Rev. Lett.* **122**, 027001 (2019).
- Drozdov, A. P. et al. Superconductivity at 250 K in lanthanum hydride under high pressures. *Nature* **569**, 528–531 (2019).
- Shaw, B. L. in *Inorganic Hydrides* 1–3 (Pergamon, 1967).
- Blackledge, J. P. in *Metal Hydrides* 1–20 (Academic Press, 1968).
- Zurek, E. Hydrides of the alkali metals and alkaline earth metals under pressure. *Comments Inorg. Chem.* **37**, 78–98 (2017).
- Zeng, Q., Yu, S., Li, D., Oganov, A. R. & Frapper, G. Emergence of novel hydrogen chlorides under high pressure. *Phys. Chem. Chem. Phys.* **19**, 8236–8242 (2017).
- Davari Esfahani, M. M. et al. Superconductivity of novel tin hydrides (SnnHm) under pressure. *Sci. Rep.* **6**, 22873 (2016).
- Peng, F. et al. Hydrogen clathrate structures in rare earth hydrides at high pressures: possible route to room-temperature superconductivity. *Phys. Rev. Lett.* **119**, 107001 (2017).
- Wang, H., Tse, J. S., Tanaka, K., Itaka, T. & Ma, Y. Superconductive sodalite-like clathrate calcium hydride at high pressures. *Proc. Natl Acad. Sci. USA* **109**, 6463–6466 (2012).
- Lonie, D. C., Hooper, J., Altintas, B. & Zurek, E. Metallization of magnesium polyhydrides under pressure. *Phys. Rev. B* **87**, 054107 (2013).
- Feng, X., Zhang, J., Gao, G., Liu, H. & Wang, H. Compressed sodalite-like MgH₆ as a potential high-temperature superconductor. *RSC Adv.* **5**, 59292–59296 (2015).
- Li, Y. et al. Pressure-stabilized superconductive yttrium hydrides. *Sci. Rep.* **5**, 9948 (2015).
- Liu, H., Naumov, I. I., Hoffmann, R., Ashcroft, N. W. & Hemley, R. J. Potential high T_c superconducting lanthanum and yttrium hydrides at high pressure. *Proc. Natl Acad. Sci. USA* **114**, 6990–6995 (2017).
- Semenok, D. V., Kvashnin, A. G., Kruglov, I. A. & Oganov, A. R. Actinium hydrides AcH₁₀, AcH₁₂, and AcH₁₆ as high-temperature conventional superconductors. *J. Phys. Chem. Lett.*, 1920–1926, <https://doi.org/10.1021/acs.jpcclett.8b00615> (2018).
- Kvashnin, A. G. et al. *ACS applied materials & interfaces* **10**, 43809–43816 (2018)
- Pépin, C. M., Geneste, G., Dewaele, A., Mezouar, M. & Loubeyre, P. Synthesis of FeH₅: a layered structure with atomic hydrogen slabs. *Science* **357**, 382–385 (2017).
- Geballe, Z. M. et al. Synthesis and stability of lanthanum superhydrides. *Angew. Chem. Int. Ed.* **57**, 688–692 (2018).
- Kruglov, I. A. et al. Uranium polyhydrides at moderate pressures: prediction, synthesis, and expected superconductivity. *Sci. Adv.* **4**, eaat9776 (2018).
- Pépin, C., Loubeyre, P., Occelli, F. & Dumas, P. Synthesis of lithium polyhydrides above 130 GPa at 300 K. *Proc. Natl Acad. Sci. USA* **112**, 7673–7676 (2015).
- Struzhkin, V. V. et al. Synthesis of sodium polyhydrides at high pressures. *Nat. Commun.* **7**, 12267 (2016).
- Somayazulu, M. et al. Pressure-induced bonding and compound formation in xenon–hydrogen solids. *Nat. Chem.* **2**, 50 (2009).
- Binns, J. et al. Formation of $\{\text{H}\}_2$ -rich iodine-hydrogen compounds at high pressure. *Phys. Rev. B* **97**, 024111 (2018).
- Crabtree, G. W., Dresselhaus, M. S. & Buchanan, M. V. The hydrogen economy. *Phys. Today* **57**, 39–44 (2004).
- Halevy, I., Salhov, S., Zalkind, S., Brill, M. & Yaar, I. High pressure study of β -UH₃ crystallographic and electronic structure. *J. Alloy Compd.* **370**, 59–64 (2004).
- Davari Esfahani, M. M., Oganov, A. R., Niu, H. & Zhang, J. Superconductivity and unexpected chemistry of germanium hydrides under pressure. *Phys. Rev. B* **95**, 134506 (2017).
- Pépin, C. M., Dewaele, A., Geneste, G., Loubeyre, P. & Mezouar, M. New iron hydrides under high pressure. *Phys. Rev. Lett.* **113**, 265504 (2014).
- Goncharenko, I. et al. Pressure-induced hydrogen-dominant metallic state in aluminum hydride. *Phys. Rev. Lett.* **100**, 045504 (2008).
- McMahon, J. M. & Ceperley, D. M. Ground-state structures of atomic metallic hydrogen. *Phys. Rev. Lett.* **106**, 165302 (2011).
- Tanaka, K., Tse, J. S. & Liu, H. Electron-phonon coupling mechanisms for hydrogen-rich metals at high pressure. *Phys. Rev. B* **96**, 100502 (2017).
- Vohra, Y. K., Beaver, S. L., Akella, J., Ruddle, C. A. & Weir, S. T. Ultrapressure equation of state of cerium metal to 208 GPa. *J. Appl. Phys.* **85**, 2451–2453 (1999).
- Carbotte, J. P., Nicol, E. J. & Timusk, T. Detecting superconductivity in the high pressure hydrides and metallic hydrogen from optical properties. *Phys. Rev. Lett.* **121**, 047002 (2018).
- Hellman, O. & Abrikosov, I. A. Temperature-dependent effective third-order interatomic force constants from first principles. *Phys. Rev. B* **88**, 144301 (2013).
- Hellman, O., Abrikosov, I. A. & Simak, S. I. Lattice dynamics of anharmonic solids from first principles. *Phys. Rev. B* **84**, 180301 (2011).
- Zhu, Q., Oganov, A. R., Lyakhov, A. O. & Yu, X. Generalized evolutionary metadynamics for sampling the energy landscapes and its applications. *Phys. Rev. B* **92**, 024106 (2015).
- Errea, I. et al. High-pressure hydrogen sulfide from first principles: a strongly anharmonic phonon-mediated superconductor. *Phys. Rev. Lett.* **114**, 157004 (2015).
- Errea, I. et al. Quantum hydrogen-bond symmetrization in the superconducting hydrogen sulfide system. *Nature* **532**, 81 (2016).
- Prakapenka, V. B. et al. Advanced flat top laser heating system for high pressure research at GSECARS: application to the melting behavior of germanium. *High. Press. Res.* **28**, 225–235 (2008).

53. Goncharov, A. F. et al. X-ray diffraction in the pulsed laser heated diamond anvil cell. *Rev. Sci. Instrum.* **81**, 113902 (2010).
54. Prescher, C. & Prakapenka, V. B. DIOPTAS: a program for reduction of two-dimensional X-ray diffraction data and data exploration. *High. Press. Res.* **35**, 223–230 (2015).
55. Glass, C. W., Oganov, A. R. & Hansen, N. USPEX—evolutionary crystal structure prediction. *Comput. Phys. Commun.* **175**, 713–720 (2006).
56. Oganov, A. R. & Glass, C. W. Crystal structure prediction using ab initio evolutionary techniques: principles and applications. *J. Chem. Phys.* **124**, 244704 (2006).
57. Lyakhov, A. O., Oganov, A. R. & Valle, M. How to predict very large and complex crystal structures. *Comput. Phys. Commun.* **181**, 1623–1632 (2010).
58. Oganov, A. R., Lyakhov, A. O. & Valle, M. How evolutionary crystal structure prediction works—and why. *Acc. Chem. Res.* **44**, 227–237 (2011).
59. Kresse, G. & Joubert, D. From ultrasoft pseudopotentials to the projector augmented-wave method. *Phys. Rev. B* **59**, 1758–1775 (1999).
60. Perdew, J. P., Burke, K. & Ernzerhof, M. Generalized gradient approximation made simple. *Phys. Rev. Lett.* **77**, 3865–3868 (1996).
61. Perdew, J. P., Burke, K. & Ernzerhof, M. Generalized gradient approximation made simple [Phys. Rev. Lett. 77, 3865 (1996)]. *Phys. Rev. Lett.* **78**, 1396–1396 (1997).
62. Blöchl, P. E. Projector augmented-wave method. *Phys. Rev. B* **50**, 17953–17979 (1994).
63. Monkhorst, H. J. & Pack, J. D. Special points for Brillouin-zone integrations. *Phys. Rev. B* **13**, 5188–5192 (1976).
64. Giannozzi, P. et al. QUANTUM ESPRESSO: a modular and open-source software project for quantum simulations of materials. *J. Phys. Condens. Matter* **21**, 395502 (2009).
65. Togo, A. & Tanaka, I. First principles phonon calculations in materials science. *Scr. Materialia* **108**, 1–5 (2015).
66. Wierzbowska, M., Gironcoli, S. D. & Giannozzi, P. Origins of low- and high-pressure discontinuities of T_c in niobium. Preprint at <https://arxiv.org/abs/cond-mat/0504077v2> (2005).
67. Allen, P. B. & Dynes, R. C. Transition temperature of strong-coupled superconductors reanalyzed. *Phys. Rev. B* **12**, 905–922 (1975).
68. Ce, M. et al. Structure phase transformation and equation of state of cerium metal under pressures up to 51 GPa. *Chin. Phys. B* **25**, 046401 (2016).
69. Lipp, M. J. et al. Comparison of the high-pressure behavior of the cerium oxides Ce_2O_3 and Ce_2O_2 . *Phys. Rev. B* **93**, 064106 (2016).
70. Jacobsen, M. K., Velisavljevic, N., Dattelbaum, D. M., Chellappa, R. S. & Park, C. High pressure and temperature equation of state and spectroscopic study of CeO₂. *J. Phys. Condens. Matter* **28**, 155401 (2016).
71. Loubeyre, P. et al. X-ray diffraction and equation of state of hydrogen at megabar pressures. *Nature* **383**, 702 (1996).

Acknowledgements

The authors thank Suyu Fu of UT Austin for his assistance for the XRD data collection, Dr. Neelam Yedukondalu for the calculation of temperature dependent phonon dispersion and Yuyong Xiong for hydrogen loading at Center for High Pressure Science and Technology Advanced Research (HPSTAR). The authors thank Saori Kawaguchi and Naohisa Hirao for the help during experiment at SPring8. J.Z., Y.W., A.O., and J.F.L. acknowledge the support from DOD-ARMY grant (W911NF-16-1-0559). M.M.D.E. acknowledges support from the National Science Foundation (EAR-1723160) for supporting this work. N.P.S. and Y.Z. acknowledge support from HPSTAR. Y.Z.

acknowledges support from “the Fundamental Research Funds for the central universities” in China (Grant No. YJ201809) and from the NSFC (Grant No. 41804082). High-pressure XRD experiments were conducted at GeoSoilEnviroCARS of APS, ANL. GeoSoilEnviroCARS operations are supported by the National Science Foundation-Earth Sciences (EAR-1128799) and the Department of Energy, Geosciences (DE-FG02-94ER14466). This research used resources of the Advanced Photon Source, a U.S. Department of Energy (DOE) Office of Science User Facility operated for the DOE Office of Science by Argonne National Laboratory under Contract No. DE-AC02-06CH11357. Calculations were mainly performed on the cluster (QSH) in our laboratory at Stony Brook University.

Author contributions

J.F.L. and N.P.S. conceived the project. J.F.L. supervised the project, and J.F.L. and N.P.S. coordinated the project. N.P.S. planned the experiment and prepared the diamond anvil cell samples. Y.Z., J.F.L., E.G. and V.B.P. carried out the XRD measurements with the laser heating at high pressures. N.P.S. analysed and modelled the data, N.P.S. and J.F.L. interpreted the initial data. M.M.D.E., I.A.K., and A.R.O. carried out the theoretical calculations. All the authors discussed the results. N.P.S. and M.M.D.E. wrote the draft. A.R.O., J.Z., and J.F.L. participated in writing and revising the manuscript, and J.Z. and J.F.L. helped with the draft abstract. Y.W., J.L. and all the authors read and commented on the manuscript.

Competing interests

The authors declare no competing interests.

Additional information

Supplementary Information accompanies this paper at <https://doi.org/10.1038/s41467-019-12326-y>.

Correspondence and requests for materials should be addressed to A.R.O. or J.-F.L.

Peer review information *Nature Communications* thanks the anonymous reviewers for their contribution to the peer review of this work. Peer reviewer reports are available.

Reprints and permission information is available at <http://www.nature.com/reprints>

Publisher's note Springer Nature remains neutral with regard to jurisdictional claims in published maps and institutional affiliations.



Open Access This article is licensed under a Creative Commons Attribution 4.0 International License, which permits use, sharing, adaptation, distribution and reproduction in any medium or format, as long as you give appropriate credit to the original author(s) and the source, provide a link to the Creative Commons license, and indicate if changes were made. The images or other third party material in this article are included in the article's Creative Commons license, unless indicated otherwise in a credit line to the material. If material is not included in the article's Creative Commons license and your intended use is not permitted by statutory regulation or exceeds the permitted use, you will need to obtain permission directly from the copyright holder. To view a copy of this license, visit <http://creativecommons.org/licenses/by/4.0/>.

© The Author(s) 2019